

CECNN: COPULA-ENHANCED CONVOLUTIONAL NEURAL NETWORKS IN JOINT PREDICTION OF REFRACTION ERROR AND AXIAL LENGTH BASED ON ULTRA-WIDEFIELD FUNDUS IMAGES

BY CHONG ZHONG^{†2}, YANG LI^{†1}, DANJUAN YANG⁴, MEIYAN LI⁴, XINGTAO ZHOU⁴,
BO FU^{‡1,a}, CATHERINE C. LIU^{‡ 2,b}, AND A.H. WELSH³

¹School of Data Science, Fudan University, ^afu@fudan.edu.cn

²Department of Applied Mathematics, The Hong Kong Polytechnic University, ^bmacliu@polyu.edu.hk

³College of Business and Economics, Australian National University

⁴Eye Institute and Department of Ophthalmology, Eye & ENT Hospital, Fudan University

Ultra-widefield (UWF) fundus images are replacing traditional fundus images in screening, detection, prediction, and treatment of complications related to myopia because their much broader visual range is advantageous for highly myopic eyes. Spherical equivalent (SE) is extensively used as the main myopia outcome measure, and axial length (AL) has drawn increasing interest as an important ocular component for assessing myopia. Cutting-edge studies show that SE and AL are strongly correlated. Using the joint information from SE and AL is potentially better than using either separately. In the deep learning community, though there is research on multiple-response tasks with a 3D image biomarker, dependence among responses is only sporadically taken into consideration. Inspired by the spirit that information extracted from the data by statistical methods can improve the prediction accuracy of deep learning models, we formulate a class of multivariate response regression models with a higher-order tensor biomarker, for the bivariate tasks of regression-classification and regression-regression. Specifically, we propose a copula-enhanced convolutional neural network (CeCNN) framework that incorporates the dependence between responses through a Gaussian copula (with parameters estimated from a warm-up CNN) and uses the induced copula-likelihood loss with the backbone CNNs. We establish the statistical framework and algorithms for the aforementioned two bivariate tasks. We show that the CeCNN has better prediction accuracy after adding the dependency information to the backbone models. The modeling and the proposed CeCNN algorithm are applicable beyond the UWF scenario and can be effective with other backbones beyond ResNet and LeNet.

1. Introduction. Ocular pathologies are highly prevalent globally, often resulting in visual impairment. The most recent epidemiological data indicates that at least 2.2 billion individuals worldwide present with impairments in visual acuity (Organization et al., 2019). The most prevalent form of visual impairment worldwide is myopia, estimated to affect approximately 130 million individuals globally (Holden et al., 2016). According to the World Health Organization, myopia exhibits high prevalence in high-income nations within the Asia-Pacific and East Asian regions, with estimated rates of 53.4% and 51.6% respectively (Organization et al., 2019). Particularly, in China, myopia is reported to affect around 600 million individuals, including more than 100 million primary and secondary school students

†: Co-first authors.

‡: Co-corresponding authors.

Keywords and phrases: Copula, Convolutional Neural Network, Multi-task learning, Myopia, Ultra-widefield fundus image, 3D medical image object.

(Wang et al., 2022). High myopia is often associated with axial length elongation and numerous complications including cataract genesis, retinal detachment, macular pathologies, and optic neuropathy (Ikuno, 2017). Given the widespread prevalence of myopia and its significant impact on health, there is an evident need for increased myopia screening.

In practice, the shortage of trained human resources and sustained financial resources pose great challenges to implementing myopia screening (Organization et al., 2019). It has been estimated that the ophthalmologist-to-patient ratio in China and India is nearly 1:100,000 and most of the ophthalmological resources are in urban areas, making people living in rural and remote areas less likely to visit an ophthalmologist (Sharma et al., 2012; Zhang et al., 2021). The lack of medical resources and the severe shortage of ophthalmologists make early screening difficult in remote areas. Fortunately, in recent years, deep learning techniques applied to fundus images have aided the diagnosis and assessment of several diseases including diabetic retinopathy (Cen et al., 2021; Kim et al., 2021) and glaucoma (Kim et al., 2020; Li et al., 2021). For myopia screening, there have been some related deep learning studies on predicting the diagnostically important quantities, the spherical equivalent (SE) and the axial-length (AL) separately (Yang et al. (2022); Oh et al. (2023)).

However, to the best of our knowledge, there is no work that jointly predicts the SE and AL, and uses these to classify high myopia status based on fundus images. Separately predicting SE and AL by multiple branches of convolutional neural networks (CNNs) may produce unsatisfactory accuracy and hinder its application in clinical practice. To fill this gap, in this paper, we propose a copula-enhanced convolutional neural network (CeCNN) framework to assist myopia screening based on the ultrawide field (UWF) fundus images collected in The Eye, Ear, Nose and Throat (Eye and ENT) Hospital of Fudan University from 2015 to 2019. The proposed CeCNN framework is flexible and general; it can be nested within popular backbone CNNs and can effectively improve the accuracy in the prediction of SE, AL, and the classification of high myopia, compared with the backbone CNNs. Our study reveals that *statistical toolkits help us understand the information within data objects better and promote feature extraction, and therefore, improve the performance of machine learning models.*

There are three motivations for the current study, the ophthalmological practice that screens myopia through cutting-edge UWF images, joint prediction of highly correlated outcomes, and enhancement of deep learning toolkits by incorporating data information extracted by statistical approaches.

1.1. Motivation 1: UWF fundus images. Our research is motivated by the successful use of fundus images in the clinical practice of ophthalmology. In clinical settings, typical fundus findings of myopia include a tessellated fundus, lacquer cracks, and focal or diffuse chorioretinal atrophy (Ohno-Matsui et al., 2019). As a result, fundus imaging is crucial for detecting complications related to myopia and may help identify factors that predict the progression of myopia (Ang et al., 2019).

There are two main types of fundus images: regular fundus images and ultrawide field (UWF) fundus images (Midena et al., 2022). Compared with the UWF fundus images, regular fundus images have some limitations. The visual range of the regular fundus image is confined to a mere 30° – 75° , offering limited insights into the peripheral retina. Moreover, regular fundus photography is a labor-intensive process demanding substantial photographic expertise and patient cooperation (Aggarwal et al., 2017). In contrast, the UWF fundus image offers a broader 200° view, making it especially advantageous for highly myopic eyes given the elevated occurrence of peripheral retinal lesions, including lattice degeneration and retinal breaks (Ang et al., 2019). Figure 1 illustrates some advantages of UWF imaging. In the figure, the orange dashed circle represents the area covered by regular fundus images. It is evident that UWF captures a significantly larger area compared to conventional fundus

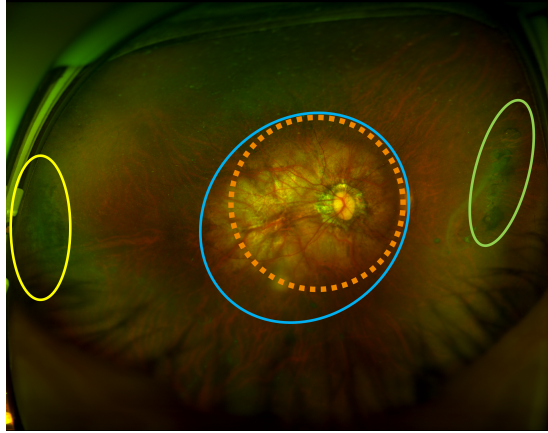


FIG 1. Advantages of UWF imaging in myopia-related pathology

images. Additionally, the area within the yellow circle indicates lesions caused by peripheral laser spots, the region within the blue circle shows extreme peripheral chorioretinal atrophy, and the area within the green circle contains pigmentary degeneration lesions. These lesions are all associated with myopia, and UWF can encompass a greater area related to myopia-associated pathologies. Hence, UWF fundus images provide much richer information than regular fundus images.

Since 2017, deep learning with UWF fundus image has been applied to diagnosing ophthalmic diseases such as glaucoma, age-related macular degeneration, and diabetic retinopathy; see [Yang et al. \(2021\)](#) for review. For myopia, we may be the first to apply deep learning to UWF fundus images to jointly predict AL, SE, and/or high myopia status.

1.2. Motivation 2: Highly correlated SE and AL. In clinical practice, SE is a key measure of the degree of myopia and determines high myopia status. Hence, predicting SE from the UWF fundus image is an indispensable task. In addition to SE, AL may be another highly relevant measure for myopia. The existing literature has shown that AL is an important ocular component which combines the information of anterior chamber depth, lens thickness, and vitreous chamber depth ([Meng et al., 2011](#); [Tideman et al., 2016](#)). An earlier study showed that AL holds significant value in predicting the onset of myopia within 2–4 years before onset ([Mutti et al., 2007](#)). When investigating refractive-error disorders, utilizing AL as a distinct trait could avoid some confounders ([Meng et al., 2011](#)). In ophthalmological practice, the association between SE and AL has been recognized as AL has been mostly regarded as a predictor for SE in high myopia screening among children ([Zhang et al. \(2011\)](#); [Zadnik et al. \(2015\)](#)). Although AL can be measured with high precision, the measurement is costly and time-consuming. Thus, predicting AL based on the UWF fundus image is meaningful. Nonetheless, existing deep learning studies with UWF fundus images either predict the AL only ([Oh et al., 2023](#)), or ignore the correlation between AL and SE and predict them separately ([Yang et al., 2022](#)).

As a matter of fact, there is a strong correlation between SE and AL. As shown by Figure 2, the scatter plot (left subfigure) reveals linear dependence between AL and SE, and the elliptical contour plot (right subfigure) indicates that the two quantities may follow a bivariate Gaussian distribution with a non-identity correlation matrix. These characteristics motivate us to model the two responses SE and AL jointly.

In addition to the two continuous quantities SE and AL, high myopia status is another essential item to be checked in myopia screening since high myopia may lead to myopic

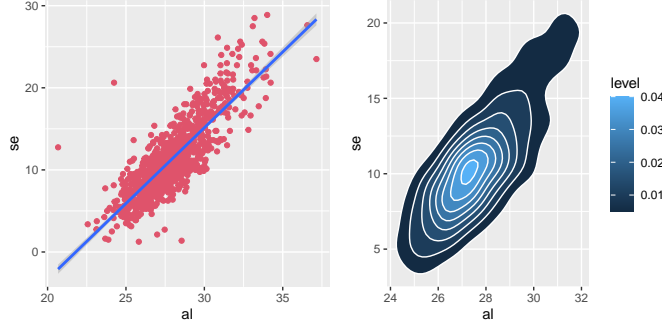


FIG 2. Left: scatter plot; right: contour plot; x axis: AL; y axis: SE.

maculopathy and substantially increase the risk of blindness (Iwase et al., 2006). To this end, in our real-world application, we categorize our tasks into regression-classification tasks and regression-regression tasks, for predicting AL (continuous variable) and high myopia status (binary variable), and predicting SE and AL, respectively. Since high myopia status is closely related to SE and so is the AL, we are driven to jointly model the two responses in both tasks.

1.3. *Motivation 3: Incorporating dependence into deep learning models.* In multi-task learning on medical images, to the best of our knowledge, dependence across the responses is rarely taken into consideration. A possible reason is that in point estimation of multivariate Gaussian mean, the maximum likelihood estimator is unrelated to the covariance/dependence structure. Hence, researchers tend to model the total loss as a weighted sum of task-specific losses such as when modeling the heteroscedastic uncertainty among the multiple tasks (Kendall et al., 2018) and using Pareto weighted multi-task learning (Lin et al., 2019), and ignore dependence modeling. Another reason may be that modeling dependence in deep learning models is non-trivial. For example, the dependence between continuous and discrete responses in regression and classification tasks may not be expressed through learnable parameters, and these may be difficult to learn by tuning due to a lack of guidance and computational infeasibility. Furthermore, incorporating dependence into a deep learning model may be sensitive to the data size. Specifically, the UWF image data was captured in The Eye and ENT Hospital of Fudan University, one of very few hospitals in mainland China with the expensive UWF imaging devices from Optomap Daytona. The data size is further limited by the high cost of diagnostic tests, making it easy to encounter the overfitting issue. Overfitting means that the dependence structure is falsely described by a huge number of redundant model parameters so the training procedure cannot incorporate the dependence information.

1.4. *Multi-response learning tasks with 3D image biomarkers.* In this paper, we consider a multi-response deep learning model with 3D image biomarkers to address our problem. Let $\mathbf{Y}_i = (y_{i,1}, \dots, y_{i,p_1}, y_{i,p_1+1}, \dots, y_{i,p_1+p_2})$ be a p -dimensional response vector, where $y_{ij} \in \mathcal{R}$ for $j \leq p_1$ and $y_{ij} \in \{0, 1\}$ for $p_1 < j \leq p_1 + p_2$. That is, there are p_1 regression tasks and p_2 binary classification tasks. Let $\mathcal{X}_i \in \mathbb{R}^{k_1 \times \dots \times k_J}$ be a J -order tensor, and $\mathcal{G} : \mathbb{R}^{k_1 \times \dots \times k_J} \rightarrow \mathbb{R}^p$ be an unknown non-linear regression function, for $i = 1, \dots, N$. We formulate the multiple-task supervised learning model for multiple *dependent* responses and a *tensor object* explanatory variable as

$$(1) \quad E(\mathbf{Y}_i | \mathcal{X}_i) = \mathcal{G}(\mathcal{X}_i) := (g_1(\mathcal{X}_i), \dots, g_p(\mathcal{X}_i)).$$

Here g_j are unknown single output functions.

We model the unknown regression functions (g_1, \dots, g_p) as p branches of CNNs, which are commonly used in deep learning to address supervised learning tasks with tensor-variate image data objects. Although there are various types of CNNs (Simonyan and Zisserman, 2014; He et al., 2016; Huang et al., 2017, among others), they share a similar architecture. In general, the architecture of a CNN consists of convolution layers, pooling layers, and fully connected layers (LeCun et al., 2015). The raw images are first fed into the convolution layer to extract the local features of the images. The local features are expressed in many feature maps by a number of filters (convolution kernels) using a convolution operator. The features extracted by a convolution layer are then aggregated in a pooling layer to merge similar features. After the above two procedures, the induced feature maps are imported to another convolution layer followed by a pooling layer through some non-linear activation function, say, the ReLU activation function (Fukushima, 1975). After a series of convolution/pooling layers, the induced features are redirected to a series of fully connected layers as ordinary deep neural networks (DNNs) to obtain the final outputs.

In general, a CNN has a huge number of parameters contained in the numerous hidden layers. Fitting a CNN is equivalent to optimizing a specific loss over these parameters. In the existing literature for multi-branch CNNs, the overall loss is usually defined as the sum of the empirical losses on all branches: the mean square error (MSE) loss of the CNNs for regression tasks and the cross entropy loss of the CNNs for classification tasks (e.g. Liu et al., 2019; Li et al., 2023, among others). However, from a statistical viewpoint, optimizing such losses ignores the inherent dependence among the responses (y_{i1}, \dots, y_{ip}) , incurring model misspecification that results in suboptimal prediction performance. This motivates us to consider a modified loss that captures the dependence structure among the multiple responses. As far as we know, there is no deep learning literature that can capture an unknown but general dependence structure in different tasks, though there is some work that considers temporal dependence across responses in facial expression analysis (Walecki et al., 2017). Particularly, if there are both classification and regression tasks, the dependence between binary and continuous responses cannot be expressed through a simple joint density function, posing a challenge to modeling the dependence structure.

In this paper, the proposed CeCNN framework sharply enhances the prediction capability of traditional CNNs in multi-response learning. The essence of the CeCNN is a so-called copula-likelihood loss that efficiently captures the dependence structure across multiple responses through a Gaussian copula model. The CeCNN framework comprises three modules, a warm-up module that trains the backbone CNNs under empirical losses, a copula estimation module that estimates the parameters in the Gaussian copula based on the results of the warm-up module, and finally, a CeCNN module that trains the backbone CNNs under the derived copula-likelihood loss. The CeCNN framework enjoys great generalizability in the sense that it is flexible to various backbone CNNs. In the application to the UWF fundus image data, CeCNN dramatically improves the prediction capability of several backbone CNNs in both regression and classification tasks, demonstrating the value of our method.

The rest of the paper is organized as follows. Sections 2 and 3 introduce how CeCNN works in regression-classification and regression-regression tasks, respectively. Section 4 presents the performance of CeCNN in prediction and classification on the UWF fundus image dataset. Section 5 carries out simulations on synthetic datasets to demonstrate CeCNN. Section 6 concludes the paper with a brief discussion about future work.

2. Regression-classification task. Due to the substantial severity of high myopia in practical scenarios and the significant role of AL in myopia prediction, this section treats the specific regression-classification task with two responses, AL and high myopia status. In medical practice, a patient is usually diagnosed with high myopia if the SE exceeds -8.0

diopters (D) (Kobayashi et al., 2005). That is, under model 1, for the i th subject, the response vector is $\mathbf{Y}_i = (y_{i1}, y_{i2})$, where $y_{i1} \in \mathbb{R}_+$ and $y_{i2} \in \{0, 1\}$ denote the AL and the status of high myopia (1: high myopia; 0, otherwise) of the i th individual, respectively. The explanatory variable is $\mathcal{X}_i \in \mathbb{R}^{224 \times 224 \times 2}$, a UWF fundus image stored in red and green with 224×224 channel-wised pixels.

In the deep learning literature, the selected loss is usually the mean square error (MSE) for *continuous responses* in regression tasks, and the cross entropy for *binary responses* in binary classification tasks. Simply optimizing the empirical losses for the CNNs for the two responses separately treats these responses as independent and thus can produce suboptimal prediction results when dependence is present. Hence, we replace the usual losses with a single *copula-likelihood* loss so that the fitted CNNs can incorporate the dependence among responses. We construct the copula-likelihood loss for the regression-classification task in subsection 2.1 and summarize the CeCNN procedure in subsection 2.2.

The copula model (Sklar (1959); Murray et al. (2013)) is an effective model for the dependence between variables. A p -dimensional copula C is a distribution function on $[0, 1]^p$, where each univariate marginal distribution is uniform on $[0, 1]$. Any joint distribution F can be completely specified by its marginal distributions and a copula, that is, there exists a copula C such that

$$F(y_1, \dots, y_p) = C\{F_1(y_1), \dots, F_p(y_p)\},$$

where F_j denotes the j th marginal CDF of y_j for $j = 1, \dots, p$. Let Φ be the CDF of the standard normal distribution and $\Gamma \equiv (\gamma_{tj})_{p \times p}$ be a correlation matrix, where the elements γ_{tj} are defined as

$$(2) \quad \gamma_{tj} = \text{corr}(\Phi^{-1}\{F_t(y_t)\}, \Phi^{-1}\{F_j(y_j)\}),$$

representing the linear correlation between two Gaussian scores $(\Phi^{-1}\{F_t(y_t)\}, \Phi^{-1}\{F_j(y_j)\})$. Equipped with the correlation matrix Γ , a Gaussian copula is given as

$$C(\mathbf{y}|\Gamma) = \Phi_p(\Phi^{-1}\{F_1(y_1)\}, \dots, \Phi^{-1}\{F_p(y_p)\}|\Gamma),$$

where $\Phi_p(\cdot|\Gamma)$ denotes the p -dimensional standard Gaussian CDF with correlation matrix Γ . Under the Gaussian copula, the coefficient γ_{tj} has a clear interpretation: when the marginal distributions F_t and F_j are Gaussian, γ_{tj} is exactly the Pearson correlation between y_t and y_j ; when F_t and F_j are both continuous but non-Gaussian, γ_{tj} is called the van der Waerden coefficient; when F_t and F_j are both discrete, the interpretation of γ_{tj} depends on the data types; see Song (2007, Section 6.3) for comprehensive descriptions.

2.1. Copula-likelihood loss. We begin by modeling the marginal distribution of $y_{i1}|\mathcal{X}_i$. Let $f_1(\cdot; g_1(\mathcal{X}_i))$ be the conditional density of $y_{i1}|\mathcal{X}_i$ so that $E(y_{i1}|\mathcal{X}_i) = g_1(\mathcal{X}_i)$. In this subsection, we assume f_1 is a Gaussian density to ease notation. That is, $y_{i1}|\mathcal{X}_i \sim N(g_1(\mathcal{X}_i), \sigma^2)$. Next, let the marginal distribution of $y_{i2}|\mathcal{X}_i$ be

$$y_{i2}|\mathcal{X}_i \sim \text{Bernoulli}[\text{Sigmoid}\{g_2(\mathcal{X}_i)\}],$$

where $\text{Sigmoid}(z) = 1/(1 + e^{-z})$. In statistics, the Sigmoid function is the inverse of the usual logit link function; in deep learning it represents a fully connected sigmoid layer applied after learning g_2 to transform the outputs to probabilities.

Let $\rho \equiv \text{corr}(\Phi^{-1}\{F_1(y_{i1})\}, \Phi^{-1}\{F_2(y_{i2})\}|\mathcal{X}_i)$ be the conditional correlation between the two Gaussian scores $\Phi^{-1}\{F_1(y_{i1})\}$ and $\Phi^{-1}\{F_2(y_{i2})\}$ (the antidiagonal of Γ). Let

$\mu_{i1} = g_1(\mathcal{X}_i)$ be the conditional expectation of y_{i1} , $\mu_{i2} = \text{Sigmoid}\{g_2(\mathcal{X}_i)\}$ be the conditional probability that $y_{i2} = 1$, and $z_{i1} = (y_{i1} - \mu_{i1})/\sigma$ be the standardized residual of y_{i1} . The partial derivative of the Gaussian copula with respect to the continuous coordinate y_{i1} is

$$\begin{aligned}
\frac{\partial}{\partial y_{i1}} C(y_{i1}, y_{i2} | \Gamma) &\propto \frac{1}{\sqrt{1-\rho^2}} \int_{-\infty}^{\Phi^{-1}(\mu_{i2})} \exp\left\{-\frac{1}{2}(z_{i1}, s)\Gamma^{-1}(z_{i1}, s)^T + \frac{1}{2}z_{i1}^2\right\} ds \\
&= \frac{1}{\sqrt{1-\rho^2}} \int_{-\infty}^{\Phi^{-1}(\mu_{i2})} \exp\left\{-\frac{z_{i1}^2 - 2\rho z_{i1}s + s^2}{2(1-\rho^2)} + \frac{z_{i1}^2}{2}\right\} ds \\
(3) \quad &= \frac{1}{\sqrt{1-\rho^2}} \int_{-\infty}^{\Phi^{-1}(\mu_{i2})} \exp\left\{-\frac{(\rho^2 z_{i1}^2 - 2\rho z_{i1}s + s^2)}{2(1-\rho^2)}\right\} ds \\
&\propto \Phi\left(\frac{\Phi^{-1}(\mu_{i2}) - \rho z_{i1}}{\sqrt{1-\rho^2}}\right) \equiv C^*(\mu_{i2}, z_{i1} | \rho).
\end{aligned}$$

A more general form of (3) for an arbitrary number of regression and classification tasks can be found in Song et al. (2009). By taking the value of y_{i2} to be either 0 or 1, the logarithm of the joint density of (y_{i1}, y_{i2}) under the Gaussian copula is

$$l(y_{i1}, y_{i2} | \mathcal{X}_i) = \log N(y_{i1}; \mu_{i1}, \sigma^2) + y_{i2} \log C^*(\mu_{i2}, z_{i1} | \rho) + (1 - y_{i2}) \log\{1 - C^*(\mu_{i2}, z_{i1} | \rho)\}.$$

Then, the copula-likelihood loss is minus the log-likelihood which is

$$\begin{aligned}
\mathcal{L}_1(g_1, p_2 | \{\mathbf{Y}_i\}_{i=1}^n, \{\mathcal{X}_i\}_{i=1}^n, \rho, \sigma) &= \frac{1}{2\sigma^2} \sum_{i=1}^n (y_{i1} - \mu_{i1})^2 \\
(4) \quad &- \left\{ \sum_{i=1}^n [y_{i2} \log C^*(\mu_{i2}, z_{i1} | \rho) + (1 - y_{i2}) \log\{1 - C^*(\mu_{i2}, z_{i1} | \rho)\}] \right\}.
\end{aligned}$$

Note that on the right hand side (RHS) of (4), the first summand is related to g_1 only, while the second summand associates μ_{i1} and μ_{i2} , or equivalently, g_1 and g_2 through a parameter ρ . Mathematically, when $\rho = 0$, $C^*(\mu_{i2}, z_{i1} | \rho)$ becomes $\mu_{i2} = \text{Sigmoid}\{g_2(\mathcal{X}_i)\}$, implying that the second summand at the RHS of equation (4) reduces to a pure cross entropy loss of g_2 only. Hence, the two nonparametric functions g_1 and g_2 (expressed in CNNs) can be learned separately. That is, by fixing $\rho = 0$, loss (4) simplifies to the sum of two empirical losses, MSE and cross entropy, as in common deep learning practice. However, when $\rho \neq 0$, g_1 and g_2 cannot be separated but have to be optimized jointly. Therefore, both σ and ρ have a substantial impact on the optimization of (4), and their effects cannot be ignored. From a statistical perspective, fixing $\rho = 0$ corresponds to treating y_{i1} and y_{i2} as conditionally independent, a strong assumption violating the data ground truth. In contrast, through the Gaussian copula, we can characterize the dependence of y_{i1} and y_{i2} by the two parameters ρ and σ , each of which has a clear interpretation.

Marginally, ρ measures the correlation between the z_{i1} , the standardized residuals of $g_1(\mathcal{X}_i)$, and the Gaussian scores $\Phi^{-1}[\text{Sigmoid}\{g_2(\mathcal{X}_i)\}]$. In this sense, specifying ρ is essential to fitting the two CNNs g_1 and g_2 . Meanwhile, note that in (4), σ^{-1} acts as the weight balancing the MSE loss and the cross-entropy-like loss. A smaller σ puts a higher weight on the MSE loss and hence, optimizing (4) may reduce the MSE prediction error if the variance of the continuous responses y_{i1} is small. This explains why in our application, in the regression-classification task of predicting AL and the status of high myopia, the CeCNN enjoys a much smaller MSE in the prediction of AL than the backbone CNNs.

2.2. *End-to-end CeCNN.* We provide the whole procedure for learning the end-to-end CeCNN in this subsection. The overall CeCNN architecture has three modules, the warm-up CNN, estimation of the copula parameters, and the CeCNN. The three modules are summarized in Algorithm 1. The plot of the CeCNN architecture can also be viewed in Fig. 5 in subsection 4.2.

Module 1 includes the basic construction of multi-branch CNNs under two empirical losses. Without loss of generality, we assume that all branches of the CNN share the same number of convolution (Conv) layers k_1 , pooling (Pool) layers k_2 , and fully connected (F-C) layers k_3 . Whether they share the same convolution or pooling layers depends on the architecture of the backbone CNN employed by the user. The last F-C layer distinguishes the tasks of regression or classification by using linear functions and the sigmoid transformation, respectively (in lines 2 and 4, respectively). Then all the numerous parameters included in the very deep layers are updated by the Adam algorithm (Kingma and Ba, 2014) to optimize the losses presented in lines 3 and 5, respectively.

In Module 2, we estimate the two copula parameters σ and ρ based on the warm-up CNN fitted in Module 1. To estimate σ , we compute the residuals from the warm-up CNN $e_i = y_{i1} - \hat{g}_1^0(\mathcal{X}_i)$ and then the sample standard deviation of the residuals. Since y_{i1} is Gaussian, the warm-up CNN \hat{g}_1^0 under the MSE loss is, marginally, the maximum likelihood estimator of g_1 . Hence, the sample standard error of the residuals is exactly the maximum likelihood estimator of σ . For estimation of the correlation ρ , we use the Pearson correlation between the Gaussian scores y_{i1} and $\Phi^{-1}(\text{Sigmoid}(g_2(\mathcal{X}_i)))$ (note that the responses y_{i1} are Gaussian). In summary, the copula parameters σ and Γ are estimated as

$$\hat{\sigma} = \text{sd}(e), \hat{\Gamma} \equiv (\hat{\rho}^{|t-j|})_{2 \times 2}, \hat{\rho} = \text{corr}(\mathbf{y}_1, \Phi^{-1}(\text{Sigmoid}(g_2(\mathcal{X}))).$$

Finally, in Module 3, we determine the copula-likelihood loss based on the estimated copula parameters and use the backbone CNNs from Module 1 to train the CeCNN under the copula-likelihood loss. Note that in this Module, CeCNN does not rely on any specific architecture in the backbone CNN, and thus, there is great flexibility in the choice of different CNNs.

3. Regression-regression task. This section treats the specific regression-regression task of predicting the clinically important, highly correlated responses SE and AL (see Figure 1), using the proposed CeCNN.

Algorithm 1 End-to-end CeCNN (regression-classification task)

Input: Training data $\{\mathcal{X}_i, \mathbf{Y}_i = (y_{i1}, y_{i2})\}_{i=1}^n$.

Output: CeCNN (\hat{g}_1, \hat{p}_2) .

Module 1: Warm-up CNN

- 1: $g_j = \text{Conv}_j(1, \dots, k_1) \circ \text{Pool}_j(1, \dots, k_2) \circ \text{F-C}_j(1, \dots, k_3)$, for $j = 1, 2$.
 - 2: $\text{F-C}_1(k_3) = \mathbf{w}_{k_3}^T \mathbf{z}_{k_3-1} + b_{k_3} = g_1(\mathcal{X}_i)$.
 - 3: $\hat{g}_1^0 = \arg \min n^{-1} \sum_{i=1}^n (y_{i1} - g_1(\mathcal{X}_i))^2$.
 - 4: $\text{F-C}_2(k_3 - 1) = \mathbf{w}_{k_3-2}^T \mathbf{z}_{k_3-2} + b_{k_3-1} \equiv g_2(\mathcal{X}_i)$, $\text{F-C}_j(k_3) = \text{Sigmoid}(g_2(\mathcal{X}_i)) \equiv p_2(\mathcal{X}_i)$.
 - 5: $\hat{p}_2^0 = \arg \min - \sum_{i=1}^n [y_{i2} \log(p_2(\mathcal{X}_i)) + (1 - y_{i2}) \log(1 - p_2(\mathcal{X}_i))]$.
-

Module 2: Estimation of copula parameters

- 6: $e_i = y_{i1} - \hat{g}_1^0(\mathcal{X}_i)$, $\hat{\sigma} = \text{sd}(e)$, $\hat{\rho} = \text{corr}(\mathbf{y}_1, \Phi^{-1}(\hat{p}_2^0(\mathcal{X})))$.
-

Module 3: CeCNN

- 7: Determine the copula-likelihood $\mathcal{L}_1(g_1, p_2 | \mathcal{X}, \mathbf{Y}, \hat{\rho}, \hat{\sigma})$ in the form of (4).
 - 8: Obtain $(\hat{g}_1, \hat{p}_2) = \arg \min \mathcal{L}_1$.
-

Let $\mathbf{Y}_i \in \mathbb{R}^p$. We rewrite model (1) as the following regression model

$$(5) \quad \mathbf{Y}_i = \mathcal{G}(\mathcal{X}_i) + \boldsymbol{\epsilon}_i,$$

where $\boldsymbol{\epsilon}_i = (\epsilon_{i1}, \dots, \epsilon_{ip})$ is a p -dimensional noise vector, $\boldsymbol{\epsilon}_i \perp \mathcal{X}_i$, $E(\epsilon_{ij}) = 0$ for all $1 \leq j \leq p$ and $\boldsymbol{\epsilon}_i \perp \boldsymbol{\epsilon}_{i'}$. Under model (5), given \mathcal{X}_i , the dependence among (Y_{i1}, \dots, Y_{ip}) is equivalent to the dependence among the noise $(\epsilon_{i1}, \dots, \epsilon_{ip})$. Therefore, the joint distribution of $\mathbf{Y}_i | \mathcal{X}_i$ can be obtained from the joint distribution of $\boldsymbol{\epsilon}_i$. Using a Gaussian copula, we obtain

$$(6) \quad F(y_{i1}, \dots, y_{ip} | \mathcal{X}_i, \Gamma) = C_p(F_{\epsilon_1}(y_{i1} - g_1[(\mathcal{X}_i)]), \dots, F_{\epsilon_p}(y_{ip} - g_p[(\mathcal{X}_i)] | \Gamma),$$

where F_{ϵ_j} denotes the marginal CDF of ϵ_j and Γ is the correlation matrix of $(\epsilon_1, \dots, \epsilon_p)$.

3.1. Two types of model error. For the regression-regression task, the key is to specify the marginal CDFs F_{ϵ_j} of the model error. In this subsection, we study two types of model error.

Gaussian error We first consider the Gaussian case where marginally, all model errors $\epsilon_j \sim N(0, \sigma_j^2)$, where σ_j is an unknown scale parameter. Then the likelihood contribution of $\mathbf{Y}_i | \mathcal{X}_i$ reduces to the multivariate Gaussian density. Hence, for some training data $(\{\mathbf{Y}_i\}_{i=1}^n, \{\mathcal{X}_i\}_{i=1}^n)$, the copula-likelihood loss may be defined as

$$(7) \quad \mathcal{L}_2(\{g_j\}_{j=1}^p | \{\mathbf{Y}_i\}_{i=1}^n; \{\mathcal{X}_i\}_{i=1}^n) = - \sum_{i=1}^n \log N_p\{(y_{i1} - g_1[(\mathcal{X}_i)], \dots, y_{ip} - g_p[(\mathcal{X}_i)]\}; \mathbf{0}_p, \Sigma\},$$

where $N_p(\cdot; \mathbf{0}_p, \Sigma)$ denotes the density of the p -variate Gaussian distribution with mean $\mathbf{0}_p$ and covariance matrix Σ . Mathematically, $\Sigma = \text{diag}(\sigma_1, \dots, \sigma_p) \Gamma \text{diag}(\sigma_1, \dots, \sigma_p) \equiv (\sigma_{tj})_{p \times p} = \gamma_{tj} \sigma_t \sigma_j$. If the correlation matrix Γ is an identity matrix, the copula-likelihood loss (7) simply reduces to the sum of the empirical MSE loss and some constant. Therefore, the copula-likelihood loss (7) is a generalization of the empirical MSE loss.

Before optimizing the loss (7) with respect to each CNN g_i , one has to estimate the covariance matrix Σ , or equivalently, the correlation Γ and the marginal standard deviations $(\sigma_1, \dots, \sigma_p)$. Intuitively, their estimates can be obtained from the empirical correlation matrix and marginal standard deviations of the residuals from warm-up CNNs. Let $(\hat{g}_{01}, \dots, \hat{g}_{0p})$ be p branches of CNNs trained with the empirical MSE loss for (g_1, \dots, g_p) on the training dataset $(\{\mathbf{Y}_i\}_{i=1}^n, \{\mathcal{X}_i\}_{i=1}^n)$. Using the residuals (e_{i1}, \dots, e_{ip}) for each observation, where $e_{ij} = y_{ij} - \hat{g}_{0j}(\mathcal{X}_i)$, we obtain estimates of the copula parameters Γ and σ_j as

$$\hat{\Gamma} \equiv (\hat{\gamma}_{tj})_{p \times p} = \text{corr}(\{e_{it}\}_{i=1}^n, \{e_{ij}\}_{i=1}^n), \quad \hat{\sigma}_j = \text{sd}(\{e_{ij}\}_{i=1}^n).$$

Here *corr* represents the Pearson correlation. With the above estimates, we can train new CNNs by optimizing the copula-likelihood loss through commonly used stochastic optimizers such as the stochastic gradient descent and the Adam algorithm (Kingma and Ba, 2014).

Nonparametric error We consider next a more general case where the marginal distribution of error ϵ_j is unknown. In this case, we estimate the marginal CDF F_{ϵ_j} for $j = 1, \dots, p$, then estimate Γ , and finally we combine them to derive the copula-likelihood loss.

Again, we begin with the warm-up CNNs with MSE loss and obtain the residuals (e_{i1}, \dots, e_{ip}) on the training dataset. The estimator of the marginal CDF F_{ϵ_j} is given by the empirical CDF of the residuals. To make sure $E(\epsilon_j) = 0$, we use the mean-centered residuals $\tilde{e}_{i1}, \dots, \tilde{e}_{ip}$ in the empirical CDF

$$\hat{F}_{\epsilon_j}(t) = \frac{1}{n} \sum_{i=1}^n I(\tilde{e}_{ij} \leq t), \quad j = 1, \dots, p.$$

To facilitate using a stochastic optimizer, we smooth the empirical CDF with a Gaussian kernel so that

$$(8) \quad \tilde{F}_{\epsilon_j}(t) = \frac{1}{n} \sum_{i=1}^n \Phi\{(t - \tilde{\epsilon}_{ij})/\psi_0\}, \quad \tilde{f}_{\epsilon_j}(t) = \frac{1}{n\psi_0} \sum_{i=1}^n \phi\{(t - \tilde{\epsilon}_{ij})/\psi_0\},$$

where $\psi_0 > 0$ is a tuning parameter.

Once we obtain the empirical estimates \tilde{F}_{ϵ_j} , the correlation matrix Γ is directly given by (2) so that

$$\hat{\gamma}_{sj} = \text{corr}(\{\Phi^{-1}(\tilde{F}_{\epsilon_s}(\tilde{\epsilon}_{is}))\}_{i=1}^n, \{\Phi^{-1}(\tilde{F}_{\epsilon_j}(\tilde{\epsilon}_{ij}))\}_{i=1}^n).$$

That is, the Pearson correlation between the two Gaussian scores of the smoothed empirical CDFs of the centered residuals.

With the above estimates, according to Song et al. (2009, eq. (7)), the copula-likelihood loss is given (up to a constant) as

$$(9) \quad \mathcal{L}_3(\{g_j\}_{j=1}^p | \{\mathbf{Y}_i\}_{i=1}^n; \{\mathcal{X}_i\}_{i=1}^n) = -\sum_{i=1}^n \frac{1}{2} \mathbf{q}_i^T (\mathbf{I}_p - \Gamma^{-1}) \mathbf{q}_i - \sum_{i=1}^n \sum_{j=1}^p \log\{\tilde{f}_{\epsilon_j}(y_{ij} - g_j(\mathcal{X}_i))\},$$

where $\mathbf{q}_i = (\Phi^{-1}\{\tilde{F}_{\epsilon_1}[y_{i1} - g_1(\mathcal{X}_i)]\}, \dots, \Phi^{-1}\{\tilde{F}_{\epsilon_p}[y_{ip} - g_p(\mathcal{X}_i)]\})^T$. Obviously, if $\Gamma = \mathbf{I}_p$ (no correlation between the responses), loss (9) reduces to the sum of minus the log densities \tilde{f}_{ϵ_j} .

3.2. End-to-end CeCNN. Finally, we summarize the CeCNN for the regression-regression task in Algorithm 2. In this task, the CeCNN again has the three-module structure with different copula parameters. For Gaussian error, the copula parameters are the marginal SDs σ_j and the Pearson correlation γ_{tj} ; for nonparametric error, the copula parameters contain an infinite dimensional parameter f_{ϵ_j} and the transformed correlation γ_{tj} . An overview of the CeCNN architecture is shown in Fig. 5 in subsection 4.2.

4. Application to the UWF fundus image dataset. For our proposed CeCNN model, in the context of the regression-classification task, we predict both the axial length and whether the patient has high myopia. Regarding the regression-regression problem, we predict the axial length and refractive error.

4.1. Data Preparation and Descriptive Analysis. The data collection process involved capturing 987 fundus images from the left eyes of 987 patients using the Optomap Daytona scanning laser ophthalmoscope (Daytona, Optos, UK). The data collection period extended from November 2015 to January 2019, and was conducted at The Eye and ENT Hospital of Fudan University. For this study, only patients with myopia in both eyes were included, and left eyes were chosen to avoid correlation between data from using both the same patient's eyes.

All enrolled patients sought refractive surgery treatment and were exclusively myopia patients. To ensure homogeneity and accuracy, individuals with other ocular conditions such as cataract, vitreoretinal diseases, or glaucoma, as well as those with a history of trauma or previous ocular surgery, were excluded from the dataset. For image selection, we required the fovea to be positioned at the center of the image and applied the criterion of gradability. Images were considered gradable if there was no blurring in the optic disc or foveal area, and if less than 50% of the peripheral retinal area was obscured by eyelids or eyelashes. The UWF fundus images obtained during the study were exported in JPEG format and compressed to a resolution of 224 x 224 pixels to facilitate subsequent analysis.

Algorithm 2 End-to-end CeCNN (regression-regression task)**Input:** Training data $\{\mathcal{X}_i, \mathbf{Y}_i = (y_{i1}, \dots, y_{ip1})\}_{i=1}^n$.**Output:** Trained CeCNN $(\hat{g}_1, \dots, \hat{g}_p)$.**Module 1: Warm-up CNN**

```

1: for  $j = 1, \dots, p$  do
2:    $g_j = \text{Conv}_j(1, \dots, k_1) \circ \text{Pool}_j(1, \dots, k_2) \circ \text{F-C}_j(1, \dots, k_3)$ .
3:    $\text{F-C}_j(k_3) = \mathbf{w}_{k_3}^T \mathbf{z}_{k_3-1} + b_{k_3} = g_j(\mathcal{X}_i)$ ;
4:    $\hat{g}_j^0 = \arg \min n^{-1} \sum_{i=1}^n (y_{ij} - g_j(\mathcal{X}_i))^2$ .
5: end for

```

Module 2: Copula parameters estimation

```

6: if Gaussian then
7:   Obtain residuals  $e_{ij} = y_{ij} - \hat{g}_j^0(\mathcal{X}_i)$ .
8:    $\hat{\sigma}_j = \text{sd}(\mathbf{e}_{ij})$ ,  $\hat{\gamma}_{tj} = \text{corr}(\mathbf{e}_{it}, \mathbf{e}_{ij})$ .
9: else if Non-Gaussian then
10:   $\tilde{e}_{ij} = e_{ij} - \bar{e}_j$ ,  $\tilde{F}_{\tilde{e}_j}(t) = \frac{1}{n} \sum_{i=1}^n \Phi_{\psi_0}(t - \tilde{e}_{ij})$ ,  $\tilde{f}_{\tilde{e}_j}(t) = \frac{1}{n} \sum_{i=1}^n \phi_{\psi_0}(t - \tilde{e}_{ij})$ 
11:   $\hat{\gamma}_{tj} = \text{corr}(\Phi^{-1}(\tilde{F}_{\tilde{e}_t}(\tilde{e}_{it})), \Phi^{-1}(\tilde{F}_{\tilde{e}_j}(\tilde{e}_{ij})))$ 
12: end if

```

Module 3: CeCNN

```

13: if Gaussian then
14:   Define the loss  $\mathcal{L}_2$  the same as (7).  $(\hat{g}_1, \dots, \hat{g}_{p1}) = \arg \min \mathcal{L}_2$ .
15: else if Non-gaussian then
16:   Define the loss  $\mathcal{L}_3$  the same as (9).  $(\hat{g}_1, \dots, \hat{g}_{p1}) = \arg \min \mathcal{L}_3$ .
17: end if

```

Response variables The response variables included in the models include two continuous responses: SE and AL, and one binary response indicating whether the patient has high myopia or not. SE and AL are recorded during the data collecting process, and high myopia is defined according to SE value. Due to the commonly observed visual dysfunction in myopic eyes with a refractive error exceeding -8.0 diopters (D), an eye is considered to have high myopia when its refractive error (the value of SE) surpasses -8.0 D. This specific value is used as the defining criterion for high myopia (Kobayashi et al., 2005). We will predict both SE and AL values (a pure regression task), and also predict AL value and myopia status (a regression-classification task). Table 1 summarizes the statistical information on SE and AL. It is clear from the table that SE and AL exhibit a strong linear correlation, suggesting that it is valuable to incorporate their dependence.

4.2. *Structure of CeCNN.* In order to demonstrate the adaptability of our model to different deep learning architectures, we selected LeNet (LeCun et al., 1998) and ResNet-18 (He et al., 2016) as our backbone models. LeNet represents one of the simplest, original CNN models, while ResNet is acknowledged as one of the most effective and prominent CNN models in the field.

TABLE 1
Statistical information of SE and AL

Variables	Range	Mean	Sd	Correlation coefficient
SE	(4.25, 23)	11.12	3.57	0.79
AL	(24.22, 34.23)	27.84	1.69	

Simplified backbone models to overcome overfitting The conventional ResNet18 model contains over ten million parameters. Similarly, when we used the traditional LeNet structure, the parameter count exceeded five million. However, our dataset comprises only a few hundred images. This discrepancy posed a significant challenge in the form of severe overfitting.

To mitigate the risk of overfitting during the training process, we adopted the common strategy of simplifying the neural network architecture. Specifically, we removed the last two CNN blocks from ResNet18 and increased the filter sizes of the convolutional and pooling layers of LeNet. This substantial reduction in the parameter count effectively prevented overfitting. After simplification, the parameter count of ResNet18 reduced from over ten million to around six hundred thousand. Similarly, the parameter count of the simplified LeNet decreased from over five million to just over sixty thousand. Fig. 3 and Fig. 4 show the architecture of the simplified versions of LeNet and ResNet18 respectively. Fig. 3 was created using (Parmar et al., 2018).

Regarding the regression-regression tasks, we observed that during the training process, when the backbone model exhibited severe overfitting, whether it was ResNet or LeNet serving as the backbone model, the CeCNN framework would fail to extract effective dependence information from the residuals. This made CeCNN ineffective. For regression-classification tasks, when LeNet was used as the backbone model, overfitting still made CeCNN ineffective. However, when ResNet was used as the backbone model, CeCNN remained effective. As a result, for regression-regression tasks, we used simplified versions of both LeNet and ResNet, and for regression-classification tasks, we applied the simplified version of LeNet and the original, unsimplified version for ResNet.

Architecture of CeCNN The complete architecture for applying the CeCNN model to the UWF dataset is illustrated in Fig. 5. Initially, we trained the backbone models and obtained the residuals from their outputs (Module 1). Then, using both the outputs and residuals, we computed estimates of the copula parameters and the correlation matrix (Module 2). With the

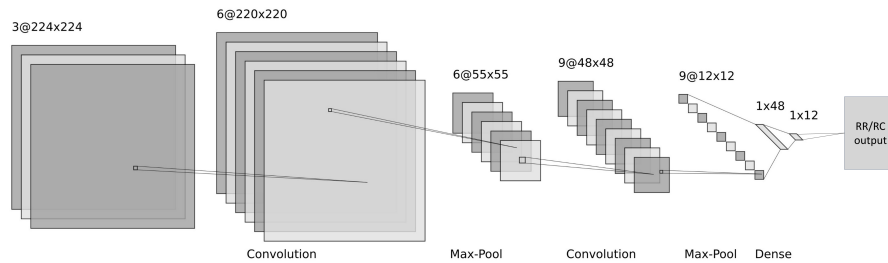


FIG 3. Architecture of simplified LeNet

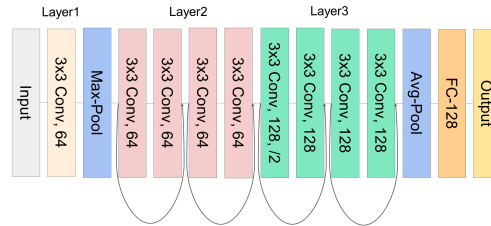


FIG 4. Architecture of simplified ResNet18

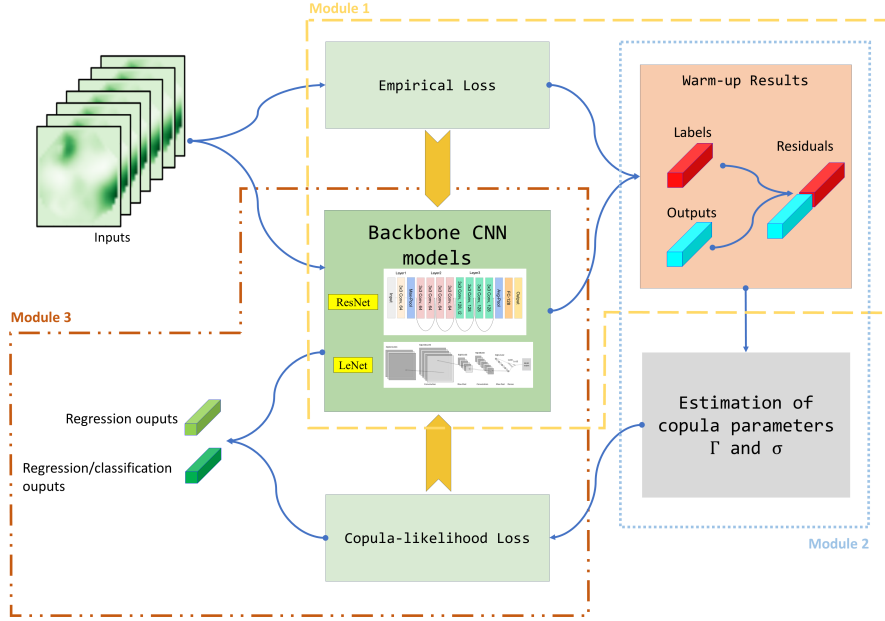


FIG 5. Architecture of proposed CeCNN.

correlation matrix and residuals, we proceeded to train our CeCNN models with the proposed copula loss (Module 3). When training our CeCNN model, we used the network parameters from the previously pre-trained CNN backbone models as the initial parameters of CeCNN.

4.3. Prediction Performance Evaluation. The dataset of 987 fundus images was partitioned into the training data set, the validation set, and the testing set, with a ratio of 6:2:2. To mitigate bias in model evaluation and obtain more reliable estimates of the results, 10 rounds of 5-fold cross-validation were employed. For the pure regression task, we calculated the Root Mean Square Error (RMSE) and the Mean Absolute Error (MAE), while for the regression-classification task, we computed the RMSE, Area Under the Curve (AUC) and accuracy. We assessed the predictive performance of our CeCNN in comparison to our backbone models, aiming to show that the proposed techniques enhance the performance of the original models.

Results of regression-classification tasks For the regression-classification tasks, the results in Fig. 6 and Fig. 7 show the enhanced predictive performance of our CeCNN models for both classification and regression tasks. When ResNet is used as the backbone model, the accuracy of predicting high myopia improves by 0.927%, but the AUC decreases by 0.065%. The RMSE for predicting AL improves by 0.913%. On the other hand, with LeNet as the backbone model, the accuracy of predicting high myopia decreases by 0.145%. However, the AUC increases by 1.227%. Simultaneously, the MSE for predicting AL improves by 1.223%.

Results of regression-regression tasks The results for the regression-regression tasks are shown in Fig. 8 and Fig. 9. Our CeCNN models demonstrate improved predictive performance for both SE and AL on average. Specifically, under the Gaussian setting, the RMSE of AL improves by an average of 10.378% and the RMSE of SE improves by an average of 0.717%, with LeNet as the backbone. On the other hand, the RMSE of AL improves by an

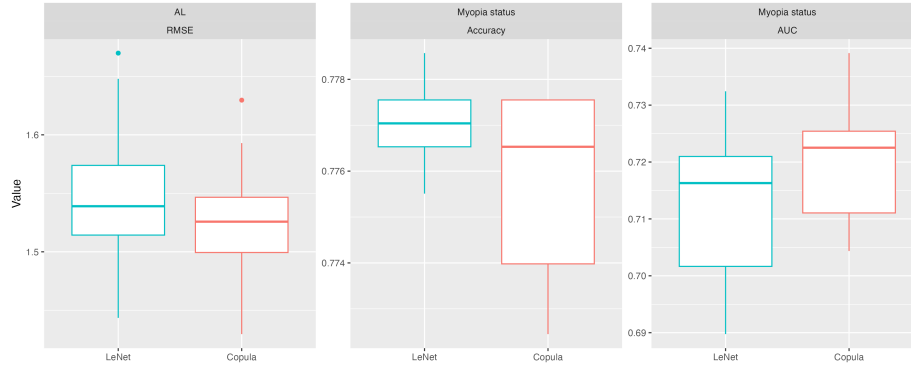


FIG 6. Box plots of MSE, Accuracy and AUC in 10 rounds of 5-fold validation of the regression-classification tasks for LeNet as the backbone model.

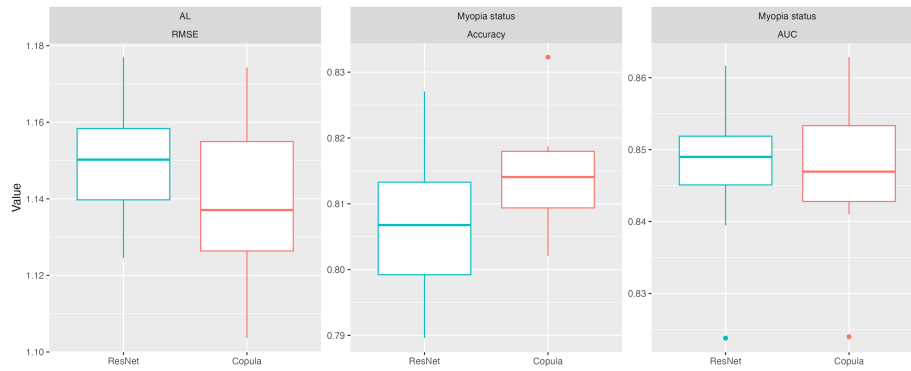


FIG 7. Box plots of MSE, Accuracy and AUC in 10 rounds of 5-fold validation of the regression-classification tasks for ResNet as the backbone model.

average of 3.683% and the RMSE of SE improves by an average of 2.232%, with ResNet as the backbone.

In the semi-parametric scenario, the RMSE of AL improves by an average of 9.905% and the RMSE of SE improves by an average of 0.528%, with LeNet as the backbone. On the other hand, the RMSE of AL improves by an average of 3.860% and the RMSE of SE improves by an average of 2.268%, with ResNet as the backbone.

5. Analysis on synthetic data. We carried out simulations of synthetic datasets for each task to demonstrate the superiority of the proposed CeCNN. To match our application scenarios, in both regression-classification and regression-regression tasks, we consider correlated bivariate responses and a single image covariate. To simplify the ground truth model, we compress the image covariate to a grey matrix. We present the simulation details for the regression-classification and regression-regression tasks in subsections 5.1 and 5.2, respectively.

5.1. Regression-classification task. On this task, the synthetic image covariate is generated as a grey matrix $X_i \in \mathbb{R}^{9 \times 9}$ that can be divided into nine independent blocks of 3×3

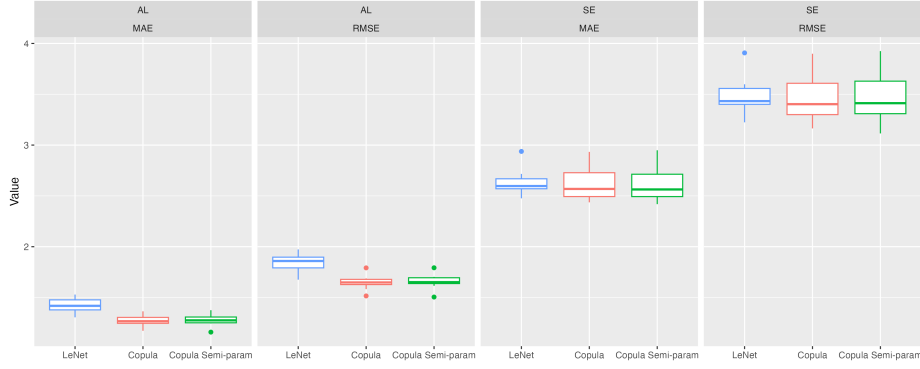


FIG 8. Box plots of RMSE and MAE in 10 rounds of 5-fold validation of the regression-regression tasks for LeNet as the backbone model.

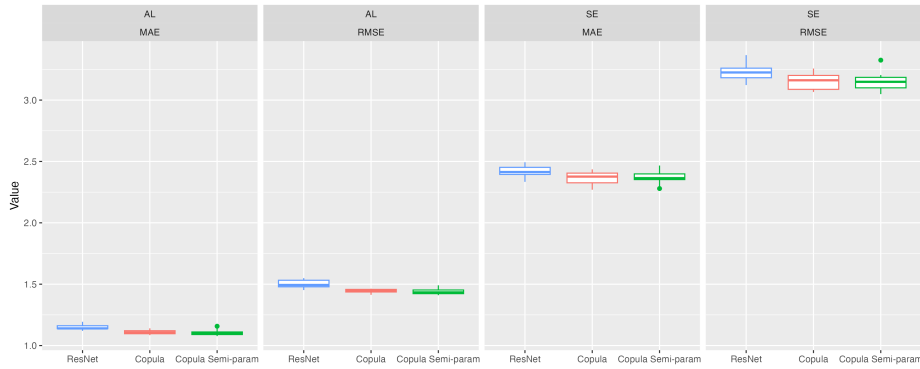


FIG 9. Box plots of RMSE and MAE in 10 rounds of 5-fold validation of the regression-regression tasks for ResNet as the backbone model.

square matrices:

$$X = \begin{pmatrix} X_{1,1} & X_{1,2} & X_{1,3} \\ X_{2,1} & X_{2,2} & X_{2,3} \\ X_{3,1} & X_{3,2} & X_{3,3} \end{pmatrix}, X_{t,s} = \begin{pmatrix} X_{t,s}^{(1,1)} & X_{t,s}^{(1,2)} & X_{t,s}^{(1,3)} \\ X_{t,s}^{(2,1)} & X_{t,s}^{(2,2)} & X_{t,s}^{(2,3)} \\ X_{t,s}^{(3,1)} & X_{t,s}^{(3,2)} & X_{t,s}^{(3,3)} \end{pmatrix}, t, s = 1, 2, 3.$$

For $k, l = 1, 2, 3$, we set $X_{3,3}^{(k,l)} \sim N(1, 0.5^2)$ as elements of the dark block and $X_{t,s}^{(k,l)} \sim N(0, 1^2)$ as elements of bright blocks, for $(t, s) \neq (3, 3)$. Based on this covariate, we generated the synthetic continuous response $y_1 \in \mathbb{R}$ and the synthetic binary response $y_2 \in \{0, 1\}$ using model (1).

For each block $X_{t,s}$, we define the block operators $S_{t,s}, S_{t,s}^* : \mathbb{R}^{3 \times 3} \rightarrow \mathbb{R}$ for responses y_1 and y_2 , respectively. Then the two responses were generated as

$$(10) \quad y_1 \sim N \left\{ \sum_{1 \leq t, s \leq 3} S_{t,s}(X_{t,s}), 1^2 \right\}, y_2 \sim \text{Bern} \left\{ \text{Sigmoid} \left[\sum_{1 \leq t, s \leq 3} S_{t,s}^*(X_{t,s}) \right] \right\}.$$

For the block operators $S_{t,s}$, we set

$$S_{1,1} = \sum_{1 \leq l, k \leq 3} \tanh(X_{1,1}^{(k,l)}), S_{2,2} = \sum_{1 \leq l, k \leq 3} X_{2,2}^{(k,l)}, S_{3,3} = \tanh \left(\sum_{1 \leq l, k \leq 3} X_{3,3}^{(k,l)} \right),$$

and $S_{t,s} = 0$ for other blocks. Under this setting, the function $g_1 = \sum_{1 \leq t, 2, \leq 3} S_{t,s}$ is a non-linear function that can be modeled by a CNN. For the block operators $S_{t,s}^*$, we set

$$S_{2,2}^* = S_{2,2} = \sum_{1 \leq l, k \leq 3} X_{2,2}^{(k,l)}$$

and $S_{t,s}^* = 0$ for other blocks so that $E(y_2) = 1/2$. The two responses are dependent in this case since they share the same block operator on block $X_{2,2}$

5.2. Regression-regression task. For the regression-regression task, we generate the synthetic image covariates in a similar way to that of the regression-classification task. For this task, we set five dark blocks $X_{t,s}^{(k,l)} \sim N(1, 0.5^2)$ for $k, l = 1, 2, 3$ and $(t, s) \in \{(1, 1), (2, 2), (3, 3), (1, 3), (3, 1)\}$. The remaining blocks are set to be the aforementioned bright blocks $N(0, 1^2)$. The responses are generated from model (5), where the model error $\epsilon_i = (\epsilon_{i1}, \epsilon_{i2}) \sim MVN(\mathbf{0}_2, \Sigma)$ with

$$\Sigma = \begin{pmatrix} 1 & 0 \\ 0 & 2 \end{pmatrix} \begin{pmatrix} 1 & 0.7 \\ 0.7 & 1 \end{pmatrix} \begin{pmatrix} 1 & 0 \\ 0 & 2 \end{pmatrix}.$$

This covariance setting yields a strong correlation and two different levels of marginal variation (variances of 1 and 4), corresponding to the AL and SE, respectively. We set the nonlinear regression functions g_1 and g_2 as the sum of block operators so that

$$g_1(X) = \sum_{1 \leq t, s \leq 3} S_{t,s}(X_{t,s}), \quad g_2(X) = \sum_{1 \leq t, s \leq 3} S_{t,s}^*(X_{t,s}).$$

The block operators $S_{t,s}$ and $S_{t,s}^*$ are defined as

$$S_{1,1} = \sum_{1 \leq l, k \leq 3} \tanh(X_{1,1}^{(k,l)}), \quad S_{2,2} = \sum_{1 \leq l, k \leq 3} X_{2,2}^{(k,l)}, \quad S_{3,3} = \tanh\left(\sum_{1 \leq l, k \leq 3} X_{3,3}^{(k,l)}\right),$$

$$S_{1,3}^* = \sum_{1 \leq l, k \leq 3} \tanh(X_{1,1}^{(k,l)}), \quad S_{2,2}^* = \sum_{1 \leq l, k \leq 3} X_{2,2}^{(k,l)}, \quad S_{3,1}^* = \tanh\left(\sum_{1 \leq l, k \leq 3} X_{3,3}^{(k,l)}\right),$$

and $S_{t,s} = S_{t,s}^*$ for the other blocks. Under this setting, marginally we have $E(y_1|X) = E(y_2|X)$ and the two regression functions g_1 and g_2 overlap.

5.3. Backbone model. A similar framework of CeCNN to that in Fig. 5 was used except that a much simpler CNN model was chosen as the backbone model for simulation. The backbone model consisted of two basic convolutional layers and two fully connected layers. The detailed architecture of the backbone model is shown in Fig. 10. For regression-classification tasks, we used MSE, AUC, and accuracy as the metrics to evaluate the results. For regression-regression tasks, we used RMSE as the metric for assessing outcomes.

5.4. Results of simulations. In total, we generated $n = 10,000$ synthetic observations in our simulations. We present the simulation results in Fig. 11 and Fig. 12. We compare the proposed CeCNN model with the backbone model only. From Fig. 11, we find that CeCNN improves prediction performance on both regression and classification tasks. Particularly, the improvement in the MSE metric on the regression task is more apparent than in the classification task. A possible reason is that the classification task is much easier in this setting since the function g_2 is actually a linear function. For regression-regression tasks, both AL and SE show remarkable improvements, with AL showing greater improvement than SE.

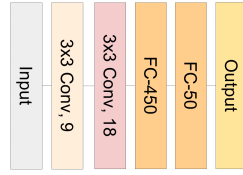


FIG 10. The architecture of CNN used in simulations.

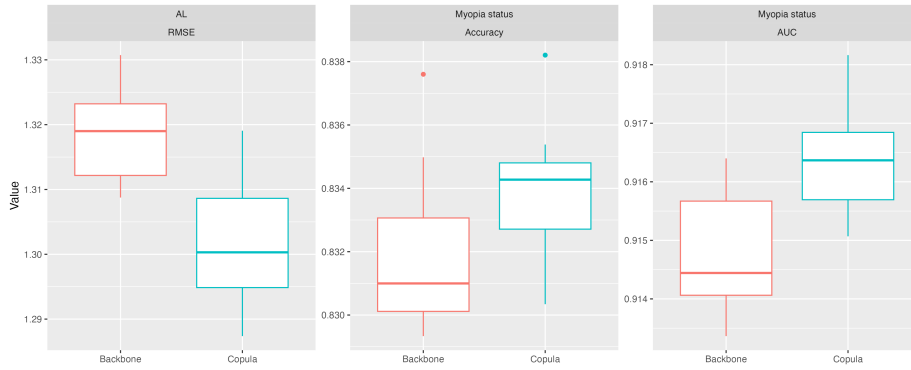


FIG 11. Box plots of MSE, Accuracy and AUC in 10 rounds of 5-fold validation of the regression-classification tasks for simulation data.

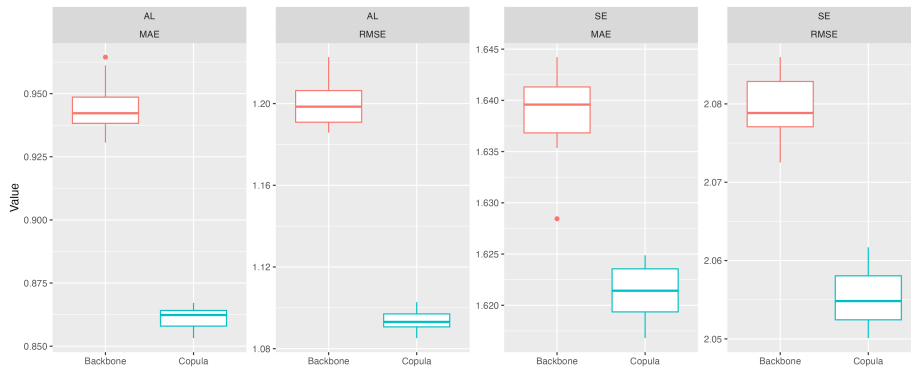


FIG 12. Box plots of RMSE and MAE in 10 rounds of 5-fold validation of the regression-regression tasks for simulation data.

6. Discussion. In this paper, we analyze one of the earliest batches of UWF fundus image data from mainland China. We succeed in enhancing the capability of deep learning models to predict AL, SE, and myopia status through our proposed CeCNN framework. In a multi-task learning scenario, CeCNN incorporates the dependence between responses into backbone CNN models through a Gaussian copula model. The use of the copula model captures the inherent dependence structure efficiently and enhances the prediction capability of deep learning models. We verify the flexibility of CeCNN using two different backbone CNNs, ResNet and Lenet. We also provide a semi-parametric alternative to the Gaussian copula for the regression-regression task, making CeCNN robust to the marginal distributions of model error.

The copula parameters may be unlearnable in the sense that they cannot be updated together with other CNN parameters in the training step. Instead, we use a warm-up CNN model to estimate them. Note that one should try to circumvent the overfitting issue in the warm-up step. Recall that in both (4) and (7), estimation of copula parameters depends on the model residuals of the regression task. An overfitted warm-up model means that all regression residuals obtained in the training procedure highly concentrate around zero and these residuals cannot provide adequate information to estimate the copula parameters. With ill-estimated copula parameters, CeCNN cannot be properly trained, let alone enhance prediction capability.

We adopt the strategy of reducing the model size, i.e. the number of CNN parameters, to circumvent overfitting; refer to subsection 4.2. Though there are other (maybe better) alternative techniques to overcome overfitting such as regularization and data augmentation (Bejani and Ghatee, 2021), we are limited by the lack of available UWF fundus image data since (the Eye and ENT Hospital of Fudan University is among the few pioneer hospitals in mainland China who deployed the Optomap Daytona devices). The huge gap between the model size and the number of subjects makes neither regularization nor data augmentation feasible as the former is sensitive to the tuning parameter and the latter is expensive without any guarantee of quality. Luckily, mainland China has been promoting the idea that departments of ophthalmology nationwide should facilitate myopia diagnostics with UWF fundus images. Once more data from multiple centers are collected, it is worthwhile and doable to explore techniques to really resolve overfitting highly over-parameterized models.

As shown in the paper, the CeCNN framework can be equipped with different types of backbone CNNs. Indeed, CeCNN does not construct a new architecture for a neural network; rather, it formulates a new loss that can be installed into any existing backbone CNNs. Furthermore, the proposed framework can be associated with various deep learning models like generative adversarial networks (Goodfellow et al., 2020) and transformers (Dosovitskiy et al., 2020). In this sense, we share a similar spirit to Kim and Wang (2023) in adapting a new loss to enhance deep learning models, though they focus on adversarial learning for multi-class classification, and we focus on multi-task learning.

Funding. Bo Fu and Yang Li are partially supported by National Natural Science Foundation of China (Grant No. 71991471). Chong Zhong is partially supported by a grant (GRF1531519) from the Research Grants Council of the Hong Kong SAR and ZZPC, PolyU. Catherine C. Liu is partially supported by a grant (GRF15301123) from the Research Grants Council of the Hong Kong SAR.

REFERENCES

- Aggarwal, K., Agarwal, A., Deokar, A., Singh, R., Bansal, R., Sharma, A., Sharma, K., Dogra, M. R., and Gupta, V. (2017). Ultra-wide field imaging in paradoxical worsening of tubercular multifocal serpiginoïd choroiditis after the initiation of anti-tubercular therapy. *Ocular Immunology and Inflammation*.
- Ang, M., Wong, C. W., Hoang, Q. V., Cheung, G. C. M., Lee, S. Y., Chia, A., Saw, S. M., Ohno-Matsui, K., and Schmetterer, L. (2019). Imaging in myopia: potential biomarkers, current challenges and future developments. *British Journal of Ophthalmology*, 103(6):855–862.
- Bejani, M. M. and Ghatee, M. (2021). A systematic review on overfitting control in shallow and deep neural networks. *Artificial Intelligence Review*, pages 1–48.
- Cen, L.-P., Ji, J., Lin, J.-W., Ju, S.-T., Lin, H.-J., Li, T.-P., Wang, Y., Yang, J.-F., Liu, Y.-F., Tan, S., et al. (2021). Automatic detection of 39 fundus diseases and conditions in retinal photographs using deep neural networks. *Nature communications*, 12(1):4828.
- Dosovitskiy, A., Beyer, L., Kolesnikov, A., Weissenborn, D., Zhai, X., Unterthiner, T., Dehghani, M., Minderer, M., Heigold, G., Gelly, S., et al. (2020). An image is worth 16x16 words: Transformers for image recognition at scale. In *International Conference on Learning Representations*.

- Fukushima, K. (1975). Cognitron: A self-organizing multilayered neural network. *Biological cybernetics*, 20(3-4):121–136.
- Goodfellow, I., Pouget-Abadie, J., Mirza, M., Xu, B., Warde-Farley, D., Ozair, S., Courville, A., and Bengio, Y. (2020). Generative adversarial networks. *Communications of the ACM*, 63(11):139–144.
- He, K., Zhang, X., Ren, S., and Sun, J. (2016). Deep residual learning for image recognition. In *Proceedings of the IEEE conference on computer vision and pattern recognition*, pages 770–778.
- Holden, B. A., Fricke, T. R., Wilson, D. A., Jong, M., Naidoo, K. S., Sankaridurg, P., Wong, T. Y., Naduvilath, T. J., and Resnikoff, S. (2016). Global prevalence of myopia and high myopia and temporal trends from 2000 through 2050. *Ophthalmology*, 123(5):1036–1042.
- Huang, G., Liu, Z., Van Der Maaten, L., and Weinberger, K. Q. (2017). Densely connected convolutional networks. In *Proceedings of the IEEE conference on computer vision and pattern recognition*, pages 4700–4708.
- Ikuno, Y. (2017). Overview of the complications of high myopia. *Retina*, 37(12):2347–2351.
- Iwase, A., Araie, M., Tomidokoro, A., Yamamoto, T., Shimizu, H., Kitazawa, Y., Group, T. S., et al. (2006). Prevalence and causes of low vision and blindness in a Japanese adult population: the Tajimi study. *Ophthalmology*, 113(8):1354–1362.
- Kendall, A., Gal, Y., and Cipolla, R. (2018). Multi-task learning using uncertainty to weigh losses for scene geometry and semantics. In *Proceedings of the IEEE conference on computer vision and pattern recognition*, pages 7482–7491.
- Kim, J. and Wang, X. (2023). Robust sensible adversarial learning of deep neural networks for image classification. *The Annals of Applied Statistics*, 17(2):961–984.
- Kim, K. E., Kim, J. M., Song, J. E., Kee, C., Han, J. C., and Hyun, S. H. (2020). Development and validation of a deep learning system for diagnosing glaucoma using optical coherence tomography. *Journal of clinical medicine*, 9(7):2167.
- Kim, K. M., Heo, T.-Y., Kim, A., Kim, J., Han, K. J., Yun, J., and Min, J. K. (2021). Development of a fundus image-based deep learning diagnostic tool for various retinal diseases. *Journal of Personalized Medicine*, 11(5):321.
- Kingma, D. P. and Ba, J. (2014). Adam: A method for stochastic optimization. *arXiv preprint arXiv:1412.6980*.
- Kobayashi, K., Ohno-Matsui, K., Kojima, A., Shimada, N., Yasuzumi, K., Yoshida, T., Futagami, S., Tokoro, T., and Mochizuki, M. (2005). Fundus characteristics of high myopia in children. *Japanese journal of ophthalmology*, 49:306–311.
- LeCun, Y., Bengio, Y., and Hinton, G. (2015). Deep learning. *nature*, 521(7553):436–444.
- LeCun, Y., Bottou, L., Bengio, Y., and Haffner, P. (1998). Gradient-based learning applied to document recognition. *Proceedings of the IEEE*, 86(11):2278–2324.
- Li, X., Lv, S., Li, M., Zhang, J., Jiang, Y., Qin, Y., Luo, H., and Yin, S. (2023). Sdmt: Spatial dependence multi-task transformer network for 3d knee MRI segmentation and landmark localization. *IEEE Transactions on Medical Imaging*.
- Li, Z., Guo, C., Lin, D., Nie, D., Zhu, Y., Chen, C., Zhao, L., Wang, J., Zhang, X., Dongye, M., et al. (2021). Deep learning for automated glaucomatous optic neuropathy detection from ultra-widefield fundus images. *British journal of ophthalmology*, 105(11):1548–1554.
- Lin, X., Zhen, H.-L., Li, Z., Zhang, Q.-F., and Kwong, S. (2019). Pareto multi-task learning. *Advances in neural information processing systems*, 32.
- Liu, M., Zhang, J., Adeli, E., and Shen, D. (2019). Joint classification and regression via deep multi-task multi-channel learning for Alzheimer’s disease diagnosis. *IEEE Transactions on Biomedical Engineering*, 66(5):1195–1206.
- Meng, W., Butterworth, J., Malecaze, F., and Calvas, P. (2011). Axial length of myopia: a review of current research. *Ophthalmologica*, 225(3):127–134.
- Midena, E., Marchione, G., Di Giorgio, S., Rotondi, G., Longhin, E., Frizziero, L., Pilotto, E., Parrozzani, R., and Midena, G. (2022). Ultra-wide-field fundus photography compared to ophthalmoscopy in diagnosing and classifying major retinal diseases. *Scientific Reports*, 12(1):19287.
- Murray, J. S., Dunson, D. B., Carin, L., and Lucas, J. E. (2013). Bayesian Gaussian copula factor models for mixed data. *Journal of the American Statistical Association*, 108(502):656–665.
- Mutti, D. O., Hayes, J. R., Mitchell, G. L., Jones, L. A., Moeschberger, M. L., Cotter, S. A., Kleinstein, R. N., Manny, R. E., Twelker, J. D., and Zadnik, K. (2007). Refractive error, axial length, and relative peripheral refractive error before and after the onset of myopia. *Investigative ophthalmology & visual science*, 48(6):2510–2519.
- Oh, R., Lee, E. K., Bae, K., Park, U. C., Yu, H. G., and Yoon, C. K. (2023). Deep learning-based prediction of axial length using ultra-widefield fundus photography. *Korean journal of ophthalmology: KJO*, 37(2):95.
- Ohno-Matsui, K., Fang, Y., Shinohara, K., Takahashi, H., Uramoto, K., and Yokoi, T. (2019). Imaging of pathologic myopia. *The Asia-Pacific Journal of Ophthalmology*, 8(2):172–177.

- Organization, W. H. et al. (2019). World report on vision.
- Parmar, C., Barry, J. D., Hosny, A., Quackenbush, J., and Aerts, H. J. (2018). Data analysis strategies in medical imaging. *Clinical cancer research*, 24(15):3492–3499.
- Sharma, T., Raman, R., John, S., and Badrinath, S. (2012). Telescreening for diabetic retinopathy in south india. *Digital Teleretinal Screening: Teleophthalmology in Practice*, pages 137–142.
- Simonyan, K. and Zisserman, A. (2014). Very deep convolutional networks for large-scale image recognition. *arXiv preprint arXiv:1409.1556*.
- Sklar, M. (1959). Fonctions de repartition an dimensions et leurs marges. *Publ. inst. statist. univ. Paris*, 8:229–231.
- Song, P. X.-K. (2007). *Correlated data analysis: modeling, analytics, and applications*. Springer.
- Song, P. X.-K., Li, M., and Yuan, Y. (2009). Joint regression analysis of correlated data using gaussian copulas. *Biometrics*, 65(1):60–68.
- Tideman, J. W. L., Snabel, M. C., Tedja, M. S., Van Rijn, G. A., Wong, K. T., Kuijpers, R. W., Vingerling, J. R., Hofman, A., Buitendijk, G. H., Keunen, J. E., et al. (2016). Association of axial length with risk of uncorrectable visual impairment for europeans with myopia. *JAMA ophthalmology*, 134(12):1355–1363.
- Walecki, R., Pavlovic, V., Schuller, B., Pantic, M., et al. (2017). Deep structured learning for facial action unit intensity estimation. In *Proceedings of the IEEE Conference on Computer Vision and Pattern Recognition*, pages 3405–3414.
- Wang, S., Dong, W., Chen, Y., Yi, Z., and Zhong, J. (2022). An automatic early screening system of eye diseases using uwf fundus images based on deep neural networks. *Intelligence-Based Medicine*, 6:100079.
- Yang, D., Li, M., Li, W., Wang, Y., Niu, L., Shen, Y., Zhang, X., Fu, B., and Zhou, X. (2022). Prediction of refractive error based on ultrawide field images with deep learning models in myopia patients. *Frontiers in medicine*, 9:834281.
- Yang, J., Fong, S., Wang, H., Hu, Q., Lin, C., Huang, S., Shi, J., Lan, K., Tang, R., Wu, Y., et al. (2021). Artificial intelligence in ophthalmopathy and ultra-wide field image: A survey. *Expert Systems with Applications*, 182:115068.
- Zadnik, K., Sinnott, L. T., Cotter, S. A., Jones-Jordan, L. A., Kleinstejn, R. N., Manny, R. E., Twelker, J. D., Mutti, D. O., et al. (2015). Prediction of juvenile-onset myopia. *JAMA ophthalmology*, 133(6):683–689.
- Zhang, M., Gazzard, G., Fu, Z., Li, L., Chen, B., Saw, S. M., and Congdon, N. (2011). Validating the accuracy of a model to predict the onset of myopia in children. *Investigative ophthalmology & visual science*, 52(8):5836–5841.
- Zhang, W., Dai, Y., Liu, M., Chen, Y., Zhong, J., and Yi, Z. (2021). Deepuwf-plus: automatic fundus identification and diagnosis system based on ultrawide-field fundus imaging. *Applied Intelligence*, 51:7533–7551.